3

Interaction of photons and neutrons with matter

3.1 Photon absorption and emission in gases

Photons interact with matter through several electromagnetic processes, with a probability determined by their energy as well as by the density and atomic number of the medium. Unlike charged particles, which release energy all along their trajectory in a trail of ionizing collisions, photons interact with matter in single encounters, with or without the creation of secondary particles. Gases are basically transparent in the visible and near ultra-violet regions; absorption begins at shorter wavelengths, in the far and vacuum ultra-violet, when the photon energy exceeds the threshold for inelastic interactions with atoms or molecules. In atomic gases, the first ionization potential defines a sharp threshold for absorption, accompanied by the emission of a photoelectron; for molecules, the presence of mechanical excitation states can lead to radiationless absorption below the photo-ionization threshold.

From the onset of absorption and up to energies of a few tens of keV, the dominant interaction process is the photoelectric effect, resulting in the release of one or more free electrons and lower energy (fluorescence) photons. Gases become gradually more transparent at photon energies exceeding a few tens of keV, and are therefore not used directly as detection media; the region of sensitivity can be extended with the use of solid converters, optimized to allow the electrons released by the interactions to enter the gaseous device and be detected. In this chapter, the absorption and photoelectric processes are discussed in detail, while the processes occurring at higher energies (Compton scattering, pair production) are only briefly mentioned.

Equally important for understanding the gas counters operation are the processes of photon emission in gas discharges, followed by absorption in the gas itself or on the counter's electrodes, often resulting in the emission of secondary electrons or photons; this subject is covered in Chapter 5.

https://doi.org/10.1017/9781009291200.005 Published online by Cambridge University Press

3.2 Photon absorption: definitions and units

The absorption of a mono-energetic beam of photons by a uniform layer of material of thickness x is described by an exponential law:

$$I = I_0 \, \mathrm{e}^{-\mu\rho x} = I_0 \, \mathrm{e}^{-\alpha x}, \tag{3.1}$$

where I_0, I are the photon fluxes entering and leaving the layer, μ the mass absorption coefficient (in cm^2/g), ρ the density of the material ($\mathrm{g/cm}^3$) and x is in cm; $\alpha = \mu\rho$ (in cm^{-1}) is the linear absorption coefficient, and represents the probability of interaction per unit length of absorber; its inverse, $\lambda = \alpha^{-1}$, is the absorption length.

Introducing in the expression the reduced material thickness $\chi = \rho x$ (in $\mathrm{g/cm}^2$):

$$I = I_0 \, \mathrm{e}^{-\mu\chi}. \tag{3.2}$$

The fraction of photons removed from the beam (the theoretical detection efficiency, if all interactions result in a visible signal) is then:

$$\varepsilon = \frac{I_0 - I}{I_0} = 1 - \mathrm{e}^{-\mu\chi}. \tag{3.3}$$

The linear absorption coefficient relates to the absorption cross section (in cm^2) through the expression:

$$\alpha = N\sigma, \tag{3.4}$$

where N is the number of atoms or molecules per unit volume:

$$N = N_\mathrm{A}\rho/A. \tag{3.5}$$

In the expression, $N_\mathrm{A} = 6.0247 \times 10^{23}$ molecules/g mole is the Avogadro number and A the atomic weight (in g/mole). For an ideal gas at STP (0 ºC, 1 atm), $N = 2.687 \times 10^{19}$ molecules/cm^3; expressing the cross section in megabarn ($1\ \mathrm{Mb} = 10^{-18}\ \mathrm{cm}^2$):

$$\alpha_\mathrm{STP}(\mathrm{cm}^{-1}) = 26.87\ \sigma(\mathrm{Mb}). \tag{3.6}$$

The linear absorption coefficient in different conditions can be computed using a density-dependent scaling law:

$$\alpha = \frac{\rho_\mathrm{STP}}{\rho}\alpha_\mathrm{STP}, \qquad \rho = P\frac{273.14}{T}\rho_\mathrm{STP}, \tag{3.7}$$

with the pressure P in atmospheres and the absolute temperature T in ºK.

For molecules, under the assumption that the constituent elements maintain their characteristics (chemical reactions can modify the optical properties at long wavelengths), the mass absorption coefficient can be deduced from the weighed sum of the individual cross sections:

https://doi.org/10.1017/9781009291200.005 Published online by Cambridge University Press

$$\mu = \frac{N_A}{M} \sum n_i \sigma_i, \tag{3.8}$$

where n_i is the number of atoms of type i and $M = \Sigma n_i A_i$ the molecular weight.

The absorption coefficient for mixtures can be obtained as the sum of the values of components weighted by their mass fraction:

$$\alpha = \sum \mu_i \rho_i. \tag{3.9}$$

The absorption cross sections and derived quantities depend on photon wavelength. Values for elements and molecules, in a wide range of energies, are scattered in a myriad of articles, and summarized in numerous textbooks and compilations, from the ultra-violet (Marr, 1967; Robin, 1974; Berkowitz, 2002) to the X- and γ-ray energies (McMaster, 1969; White-Grodstein, 1957). Recent compilations are also available on-line (Berger *et al.*, 1998; Henke *et al.*, 1993; Thompson, 2004). A variety of units have been used in the literature to describe absorption processes, generally with the purpose of providing values not too dependent on atomic number and density; some are summarized here (units are given in the GGS system):

the absorption length $\lambda = 1/\alpha$ in cm;
the mass absorption coefficient μ (often improperly called cross section) in cm^2/g;
the absorption cross section σ, in cm^2, barn (1 barn = $10^{-28} m^2$) or Megabarn (1Mb = 10^{-18} cm^2). In view of expression (3.4), the cross section is often named 'per atom' or 'per molecule';
the molar extinction coefficient η, in litres/mole cm, defined through the expression:

$$\eta = \frac{M}{x} \log_{10} \frac{I}{I_0}, \tag{3.10}$$

where M is the molar volume (litres/g mole) and x the thickness of the absorber (in cm). The extinction coefficient relates to the absorption coefficient through the expression:

$$\eta = M\alpha \log_{10} e. \tag{3.11}$$

For an ideal gas at STP, $M = 22.42$ litres/g mole; combining the previous expressions:

$$\sigma(\text{Mb}) = 3.826 \times 10^{-3} \eta. \tag{3.12}$$

The absorption cross sections, and therefore all other quantities, are a function of the photon wavelength λ (or of its energy E). Throughout this section we have preferred to use the photon energy as variable; the corresponding wavelength can be derived from:

$$\lambda(\text{nm}) = 1240/E(\text{eV}). \tag{3.13}$$

https://doi.org/10.1017/9781009291200.005 Published online by Cambridge University Press

3.3 Photon absorption processes: generalities

As an example, Figure 3.1 shows, in a wide range, the energy dependence of the absorption cross section of photons in tungsten, redrawn from data in Thompson (2004) between 10 and 1000 eV, and from White-Grodstein (1957) for higher energies.

For low to intermediate energies above the material's ionization threshold photoelectric absorption dominates, with distinctive jumps when the photon energy exceeds the various electronic shell levels. The result of the interaction is the emission of a photoelectron with a characteristic energy equal to the difference between the initial and the shell energy, accompanied by a cascade of lower energy photons or electrons resulting from the return of the atom to the ground state.

Towards higher energies, the absorption process is gradually dominated by Compton scattering, the diffusion of the incoming photon by a quasi-free electron in the atom; in coherent (or Raleigh) scattering the atom is left in the ground state, while for incoherent Compton scattering the outcome is the appearance of a lower energy photon and of an electron, emitted in a wide angular range with an energy sharing determined by conservation laws.

When the photon energy exceeds twice the mass of the electron (1.02 MeV), the process of pair production in the nuclear field of the material opens up and

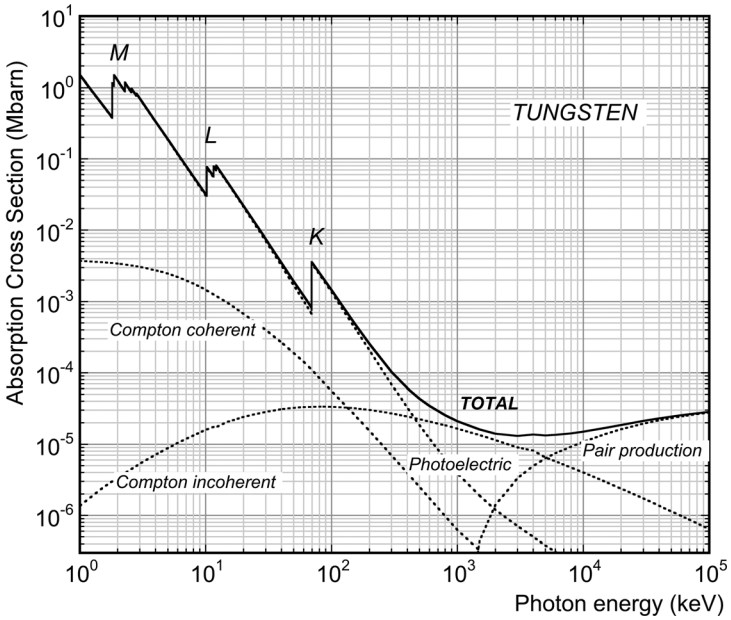

Figure 3.1 Photon absorption cross section for tungsten. Data from Thompson (2004) and White-Grodstein (1957).

https://doi.org/10.1017/9781009291200.005 Published online by Cambridge University Press

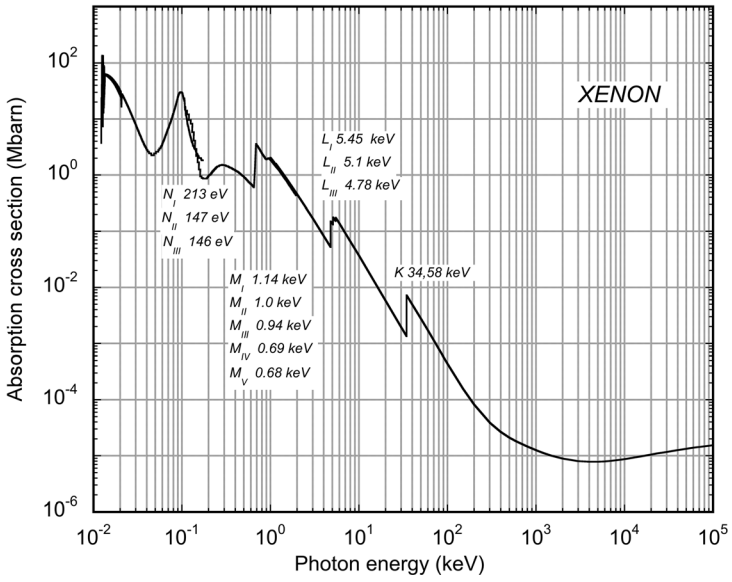

Figure 3.2 Photon absorption cross section for xenon. Data from McMaster (1969); Henke *et al.* (1993); Massey *et al.* (1969).

becomes gradually dominant, resulting in the disappearance of the photon and the creation of an electron–positron pair; appropriate energy and momentum conservation laws determine the correlations between angles and energies of the pair.

For gaseous detectors, only the domain extending from the near ultra-violet to the hard X-rays is of practical concern. For atomic gases, in this region and above the ionization potential, the dominant process is photo-ionization; Figure 3.2 provides the absorption cross section for xenon between 10 eV and 1 MeV, compiled from different sources (McMaster, 1969; Henke *et al.*, 1993; Massey *et al.*, 1969). A slight mismatch is seen between the sets of data coming from different sources.

Xenon is transparent to photons up to the first ionization potential (12.1 eV); above, the cross section reaches a maximum and decreases with upward jumps when crossing the energy levels of the various electronic shells. The region between 10 and 100 eV corresponds to the near, far and vacuum ultra-violet domain, while the X-ray region begins above 100 eV.

Knowledge of the absorption cross section for a given material permits one to estimate, using expressions (3.1) to (3.3), both the losses in the detector windows and the theoretical maximum efficiency of photon detection as a function of wavelength. As an example, Figure 3.3 shows the computed detection efficiency of a 1 cm thick counter filled with several gases at STP. Modulated by the onset of the absorption edges, it decreases from 100% at low photon energy to a few per cent

https://doi.org/10.1017/9781009291200.005 Published online by Cambridge University Press

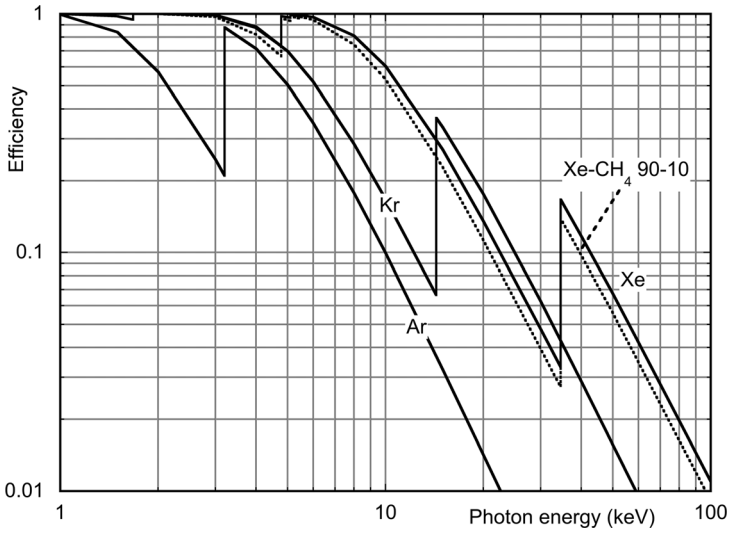

Figure 3.3 X-ray conversion efficiency in 1 cm of several gases at STP.

at shorter wavelengths. Addition to noble gases of organic quenchers, due to their smaller cross sections, results in a reduction of efficiency corresponding to an equivalent decrease of the effective mass of the main component, as shown for the Xe-CH_4 mixture.

At increasing energies, the fast decrease in conversion efficiency of gases can be partly compensated by the use of heavier molecules, thicker volumes or higher pressures. Alternatively, solid converters can be placed in front of the active volume, detecting the products of the interaction in the gas. For tungsten at 511 keV, the photon energy relevant in positron emission tomography (PET) imaging, the linear absorption coefficient is about 3 cm^{-1}, almost equally shared between photoelectric and Compton (Figure 3.1). From expression (3.2), one can infer that in a 100 μm tungsten foil about 3% of the photons interact; this is the upper limit for efficiency, assuming that all interactions result in the release of detectable ionization in the gas. As the thickness of the foil increases, so does the efficiency of conversion, but the electron ejected by photoelectric or Compton effect has a fading chance of emerging into the gas and being detected. To achieve a high conversion efficiency and at the same time a good charge extraction probability, multi-layer stacks of thin converters with open gas channels designed to collect the ionization charge have been developed for the so-called heavy drift chamber, see Section 3.8 (Jeavons *et al.*, 1975).

The occurrence of a specific absorption process affects the response of detectors. When the conversion is photoelectric, the emitted electron carries a well-defined fraction of the incident photon energy, thus permitting its wavelength to be deduced. In Compton scattering, on the other hand, the ejected electron energy

https://doi.org/10.1017/9781009291200.005 Published online by Cambridge University Press

depends on its emission angle, generally unknown; at best, a detector can localize the primary interaction point, but has no energy resolution. Further interactions within the detecting medium of the scattered photon complicate the issue.

3.4 Photon absorption in gases: from the visible to the near ultra-violet domain

Gases are transparent below their absorption threshold, but owing to the fast increase and large value of the cross section they quickly become opaque above; for many practical purposes, the knowledge of the absorption curve for a known thickness, such as those shown in Figure 3.4 (Lu and McDonald, 1994), is sufficient to determine their role in the counter action.

In atomic gases, absorption occurs above a well-defined threshold corresponding to the lowest ionization potential (the energy of the valence electron), and always results in the emission of a photoelectron. The process of photo-absorption is associated with the jump of an orbital electron to a higher energy state, followed by internal rearrangements bringing the atom back to the ground state with the emission of lower energy photons or electrons. When the energy of the absorbed photon exceeds the ionization potential of the atom or molecule, the outcome of the interaction can be the ejection in the medium of a free electron; the atom or

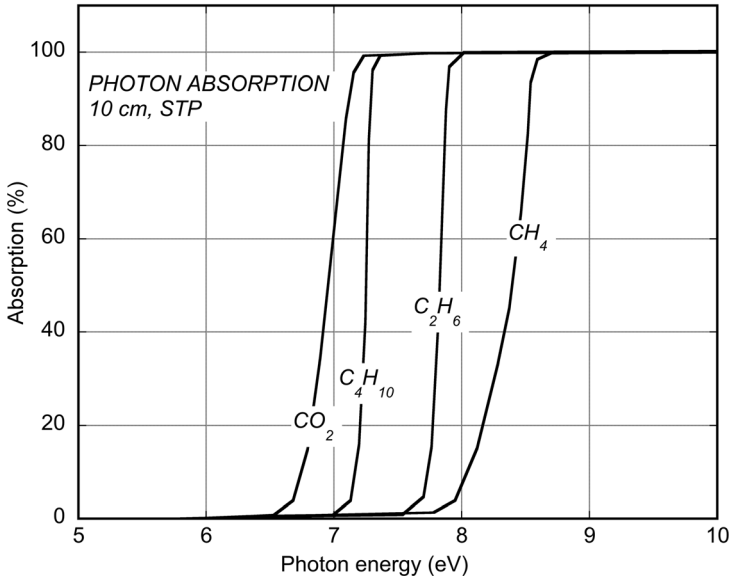

Figure 3.4 Photon absorption curves for several gases (Lu and McDonald, 1994). By kind permission of Elsevier.

https://doi.org/10.1017/9781009291200.005 Published online by Cambridge University Press

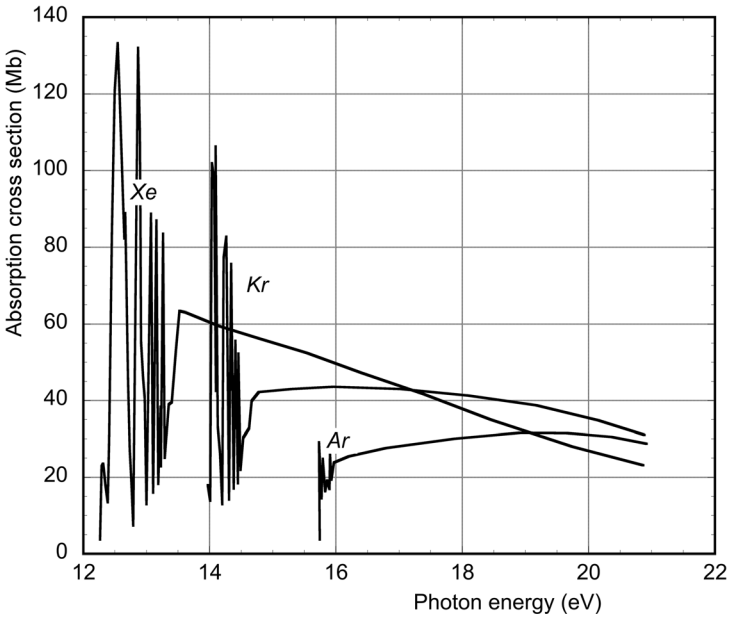

Figure 3.5 Absorption cross sections for argon, krypton and xenon. Data from Huffman *et al.* (1955).

molecule is left in an excited state, and returns to the ground state through a single transition or a cascade of processes.

In molecular gases, the presence of vibrational and rotational excited states may lead to the absorption of the photon without emission of radiation; the absorption cross section begins well before the ionization potential, and has a broad and structure-free spectrum. To dissipate the excess energy, the molecule can dissociate or return to the ground state through radiationless processes.

Comprehensive compilations of cross sections for absorption and ionization in atomic and molecular gases can be found in many textbooks and review articles (Marr, 1967; Massey *et al.*, 1969; Christophorou, 1971; Robin, 1974; Berkowitz, 2002). Values from different sources sometimes disagree; this may be due to different methods of measurement, or to the presence of trace pollutants in the gas.

For atomic gases, absorption begins sharply at the ionization potential, and continues with a broad multi-line structure until reaching a continuum; the behaviour for argon, krypton and xenon is shown in Figure 3.5 (Huffman *et al.*, 1955). Figure 3.6 and Figure 3.7 provide the absorption cross section for saturated hydrocarbons (Au *et al.*, 1993), alcohols (Robin, 1974) and dimethyl ether (DME) (Calvert and Pitts, 1966).

Figure 3.8 is the absorption cross section for water (Watanabe and Zelikoff, 1953), oxygen (Friedman, 1960), ozone (Tanaka *et al.*, 1953); Figure 3.9 for

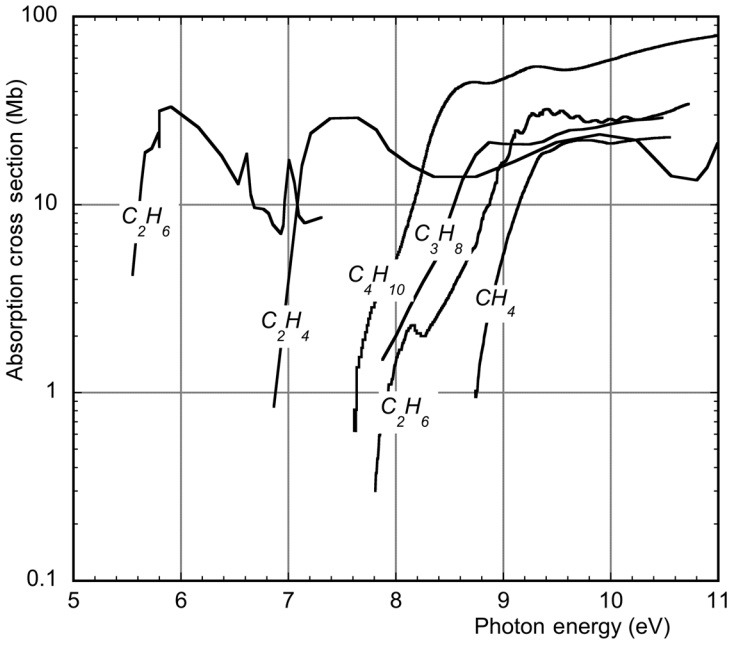

Figure 3.6 Absorption cross sections for hydrocarbons. Data from Au *et al.* (1993). By kind permission of Elsevier.

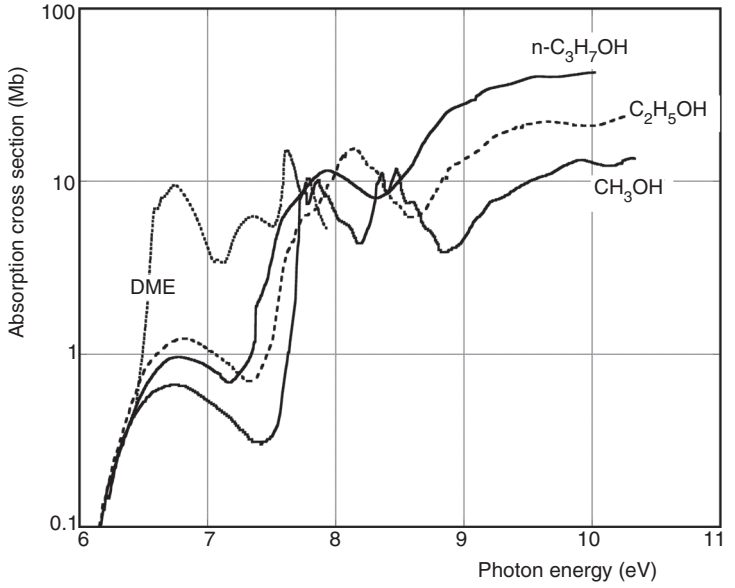

Figure 3.7 Absorption cross section for several vapours and alcohols. Author's compilation from data in different sources: dimethyl ether (Calvert and Pitts, 1966) and alcohols (Au *et al.*, 1993).

https://doi.org/10.1017/9781009291200.005 Published online by Cambridge University Press

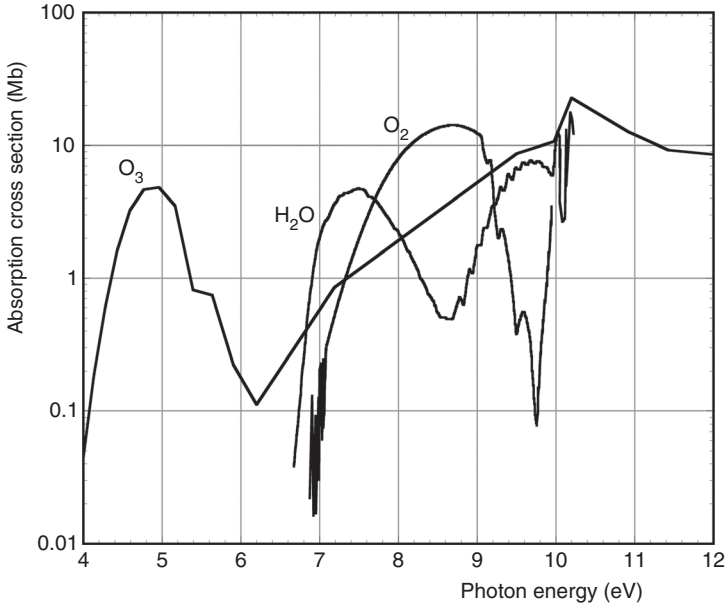

Figure 3.8 Absorption cross section for several gases. Compilation from various sources: water (Watanabe and Zelikoff, 1953), oxygen (Friedman, 1960) and ozone (Tanaka *et al.*, 1953). By kind permission of the American Optical Society.

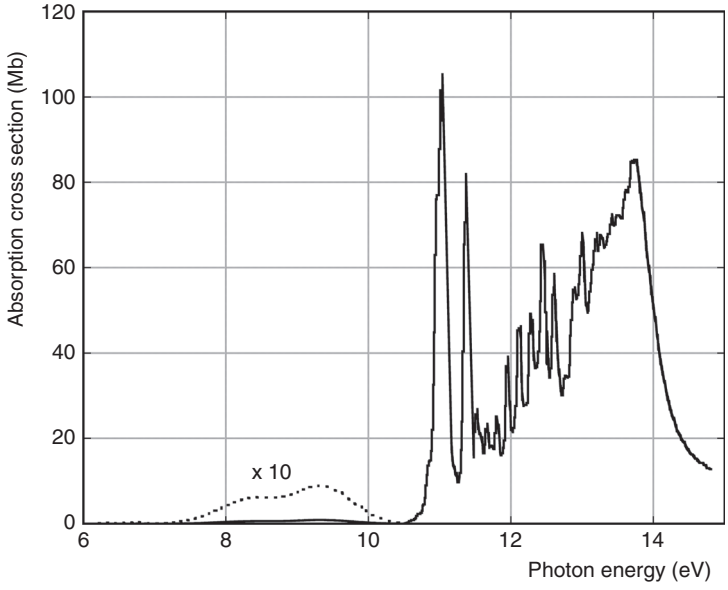

Figure 3.9 Absorption cross section for carbon dioxide (Chan *et al.*, 1993a). By kind permission of Elsevier.

https://doi.org/10.1017/9781009291200.005 Published online by Cambridge University Press

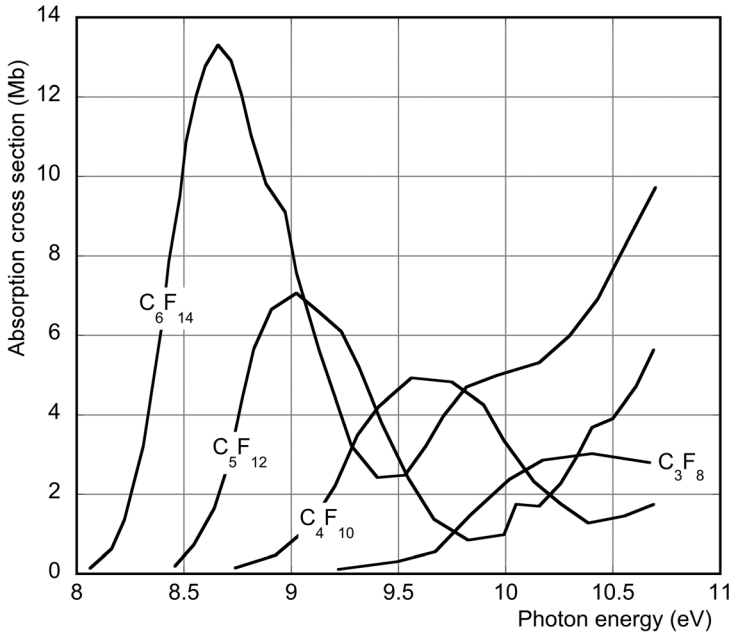

Figure 3.10 Absorption cross sections for fluorinated carbon compounds (Bélanger *et al.*, 1969). By kind permission of Elsevier.

carbon dioxide (Chan *et al.*, 1993a). Of particular relevance are the values for water and oxygen, the most common pollutants in a detector; ozone is produced in the avalanches and can affect the performances at very high rates due to its electronegativity. Figure 3.10 shows the absorption cross section in gaseous fluorinated carbon compounds (Bélanger *et al.*, 1969); freons are used as additives in detectors as well as radiators in Cherenkov ring imaging.

Figure 3.11 provides the absorption cross section for carbon tetrafluoride (CF_4) (Zhang *et al.*, 1989) and nitrogen (Chan *et al.*, 1993b).

By mixing species, one can cover a wide region of photon absorption, extending well into the near ultra-violet, and design a gas filling effectively quenching photon-mediated propagation processes; such mixtures are currently used to achieve high stable gains in proportional counters, and more recently in spark and resistive plate counters (see Chapter 12).

3.5 Photo-ionization: near and vacuum ultra-violet

Gaseous counters have only sporadically been used for detection of low energy photons, due to the limited wavelength coverage between the ionization potential and the cut-off of available detector windows. The field has been revitalized by the

https://doi.org/10.1017/9781009291200.005 Published online by Cambridge University Press

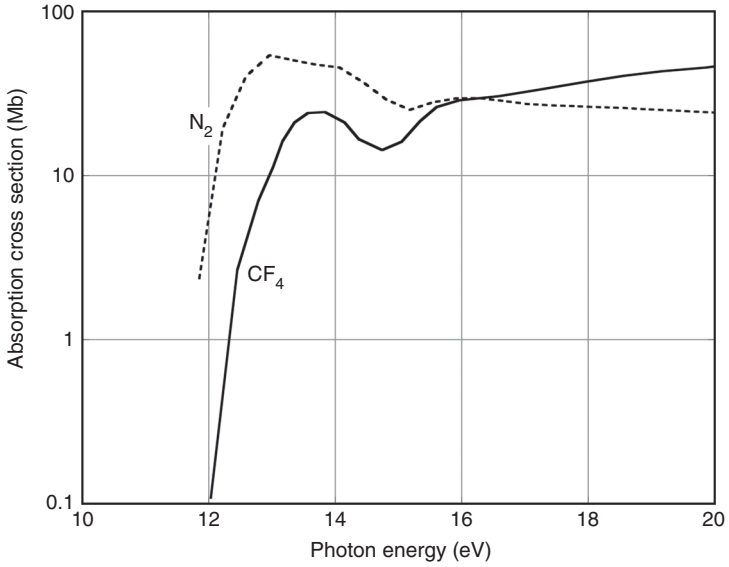

Figure 3.11 Absorption cross section for nitrogen (Chan *et al.*, 1993b) and carbon tetrafluoride (Zhang *et al.*, 1989). By kind permission of Elsevier.

development of particle identification methods based on the imaging of the pattern generated in suitable radiators by the Cherenkov effect (see ring imaging Cherenkov counters, Chapter 14); this has led to an intensive search of vapours with low ionization potential, which added to a main gas constituent extend the spectral response and therefore the detection efficiency. Absorption and photo-ionization cross sections of vapours used for UV photon detection are shown in Figure 3.12 for triethyl-amine, $(C_2H_5)_3N$ (TEA) and Figure 3.13 for tetrakis dimethyl amino ethylene $C_2[(CH_3)_2N]_4$ (TMAE) (Holroyd *et al.*, 1987).[1]

For completeness, although not used in a vapour phase, Figure 3.14 gives the quantum efficiency of caesium iodide, employed as thin-layer internal photo-cathode in several detectors, in particular for Cherenkov ring imaging (RICH) devices (Séguinot *et al.*, 1990).

Not only can photons from external sources be converted into charge and detected, but the development and spread of the signals in gaseous counters can be largely dominated also by photon emission and absorption processes. At high electric fields, photons in the ultra-violet region are copiously emitted by the inelastic collisions of electrons with atoms and molecules; depending on their wavelength, they can be absorbed or reconvert into secondary electrons, both in the gas and on the detector electrodes, spreading the original charge and often

[1] Cross section values and detailed shapes of the curves depend on the source.

https://doi.org/10.1017/9781009291200.005 Published online by Cambridge University Press

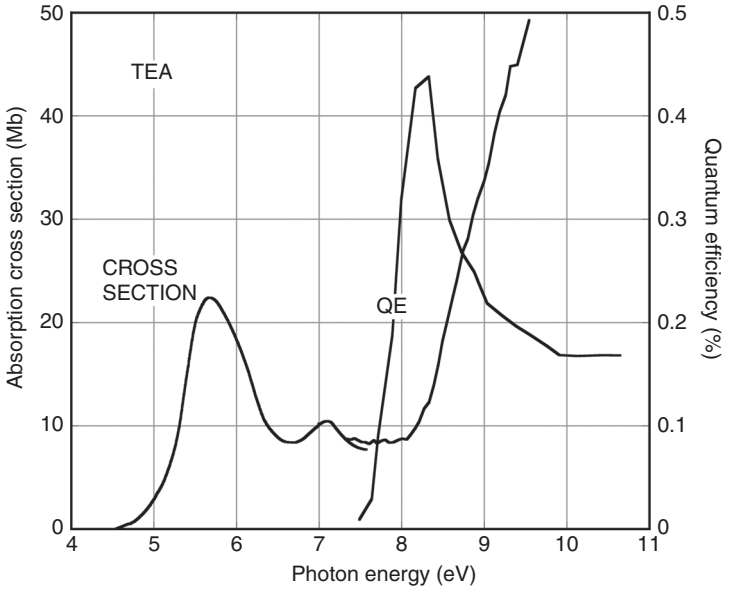

Figure 3.12 Absorption cross section and photo-ionization efficiency for triethyl amine (TEA) (Holroyd *et al.*, 1987). By kind permission of Elsevier.

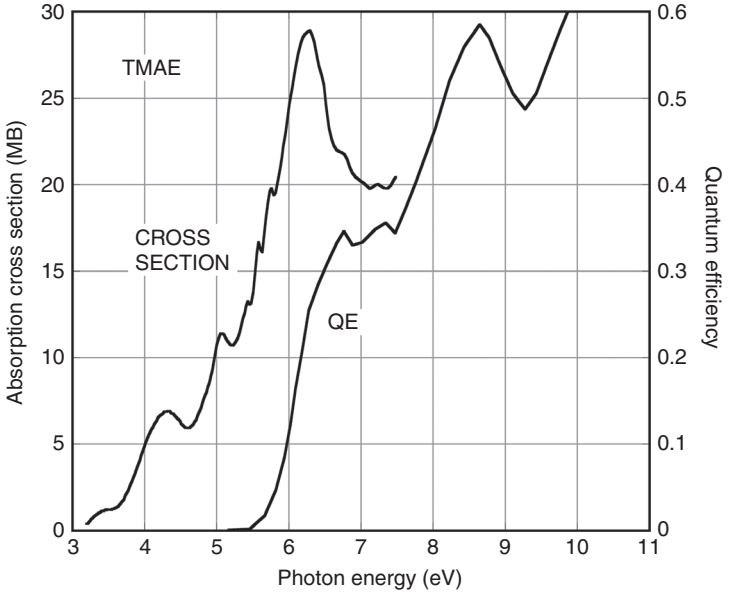

Figure 3.13 Absorption cross sections and photo-ionization efficiency for TMAE (Holroyd *et al.*, 1987). By kind permission of Elsevier.

https://doi.org/10.1017/9781009291200.005 Published online by Cambridge University Press

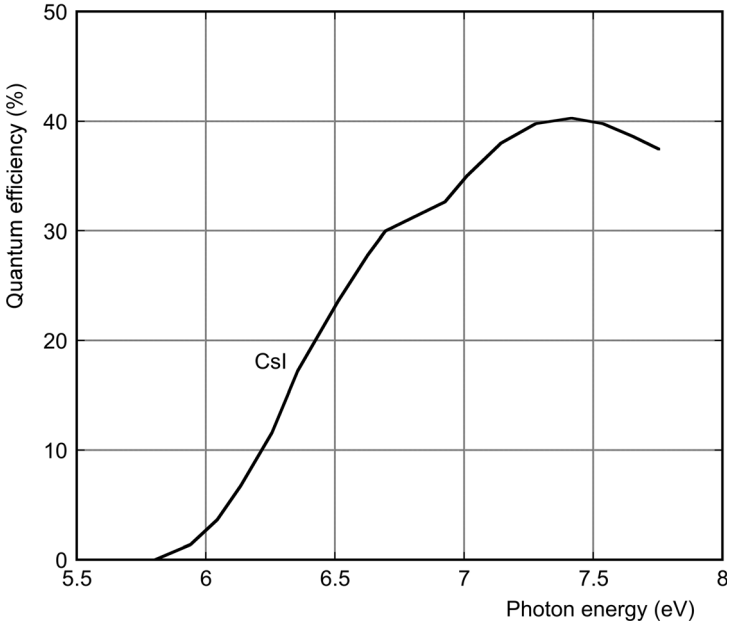

Figure 3.14 Quantum efficiency of caesium iodide (Séguinot *et al.*, 1990). By kind permission of Elsevier.

leading to discharge. An extreme case is the Geiger counter, where the discharge propagates through all the gas volume. As discussed in Chapter 5, the non-radiative absorption properties of molecular gases play a fundamental role in controlling the operating properties of counters, in particular permitting one to reduce the signal spread and to attain large charge gains.

3.6 Photo-ionization in the X-ray region

The X-ray absorption is a quantum process involving one or more transitions in the electron shells of a molecule. Denoting by E_j the binding energy of a shell j, photoelectric absorption in the shell takes place only for photon energies $E_0 > E_j$; at a given energy, the contributions of all levels having $E_j < E_0$ add up with a probability determined by the respective cross sections. The absorption reaches a maximum just above the shell level, and then rapidly decreases with energy. The binding energy of a given shell increases with the atomic number, as shown in Figure 3.15; precise numerical values can be found in textbooks and tables (McMaster 1969; Thompson, 2004). Figure 3.16 is a compilation photo-ionization cross section for noble gases in the X-ray energy range from one to one hundred keV; Figure 3.17 shows the cross section for some molecular gases used in a

https://doi.org/10.1017/9781009291200.005 Published online by Cambridge University Press

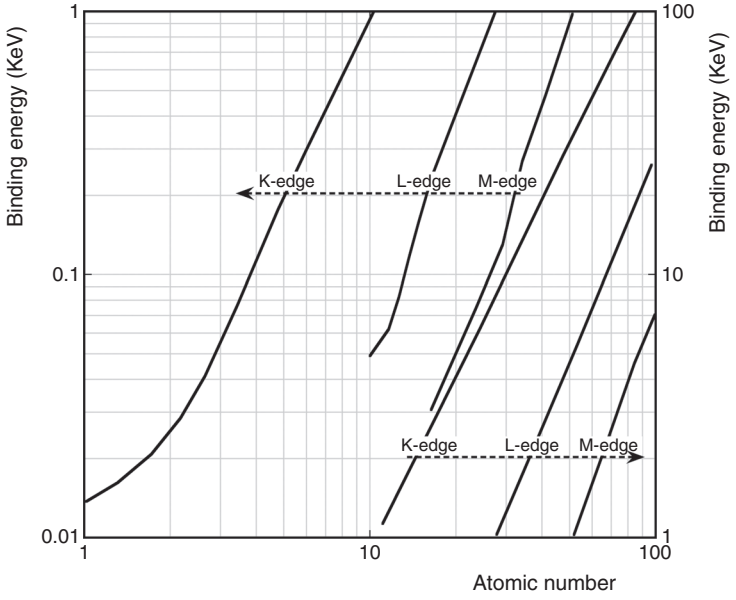

Figure 3.15 Binding energy as a function of atomic number.

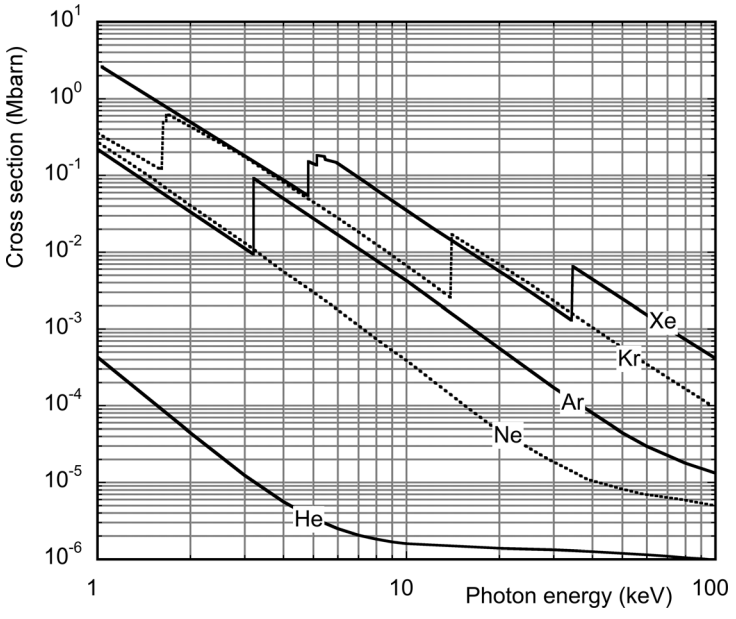

Figure 3.16 Photon total cross section for noble gases.

https://doi.org/10.1017/9781009291200.005 Published online by Cambridge University Press

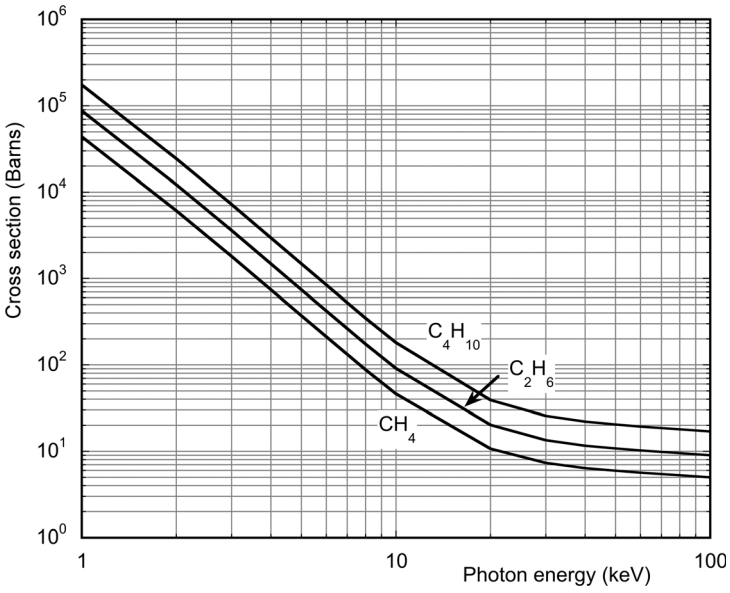

Figure 3.17 Total cross section for saturated hydrocarbons.

proportional counter, computed using the data for carbon and hydrogen in the quoted tables and expression (3.8). As already mentioned, in the mixtures of a noble gas and a hydrocarbon quencher used in gaseous counters, the contribution of the additives to photon absorption in the X-ray domain is negligible, but proper account should be taken of the reduction of the effective mass of the main constituent.

From (3.6), one can compute the mean free path for absorption in gases at standard conditions (STP), shown in Figure 3.18; appropriate composition rules can be used for mixtures (expression (3.9)).

Following the photoelectric absorption, the excited molecule can return to the ground state through two competing mechanisms:

fluorescence: transition of an electron from an energy shell $E_i < E_j$ into the j-shell, with the emission of a photon of energy E_j - E_i;

Auger effect: an internal rearrangement involving several electrons from the lower energy shells, with the emission of one or more electrons of total energy close to E_j.

The fraction of de-excitations resulting in the emission of a photon is named fluorescence yield; its value increases with the atomic number, as shown in Figure 3.19 for K-edge absorptions (Broyles *et al.*, 1953). In argon, for example, about 8% of the photoelectric absorptions are accompanied by the emission of a photon, while in 92% of the events, together with the photoelectron, one or more

https://doi.org/10.1017/9781009291200.005 Published online by Cambridge University Press

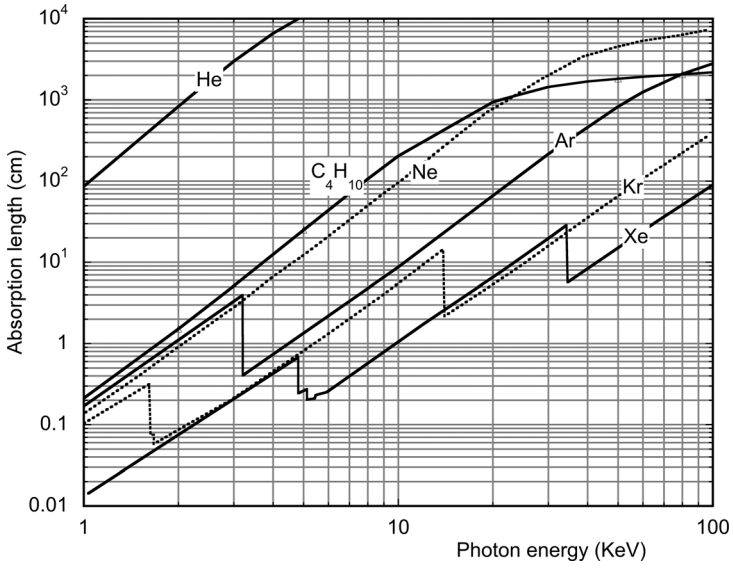

Figure 3.18 Absorption length for gases at STP.

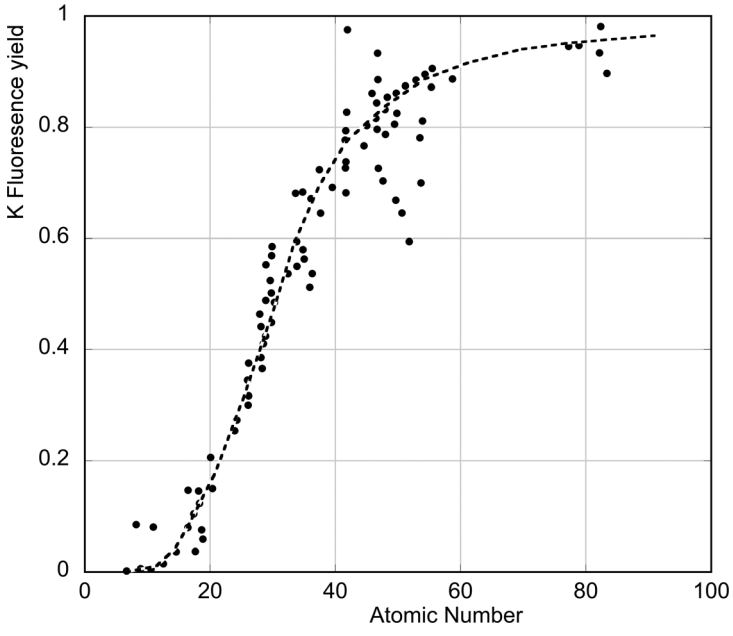

Figure 3.19 K-edge fluorescence yield as a function of atomic number (Broyles *et al.*, 1953). By kind permission of the American Physical Society.

https://doi.org/10.1017/9781009291200.005 Published online by Cambridge University Press

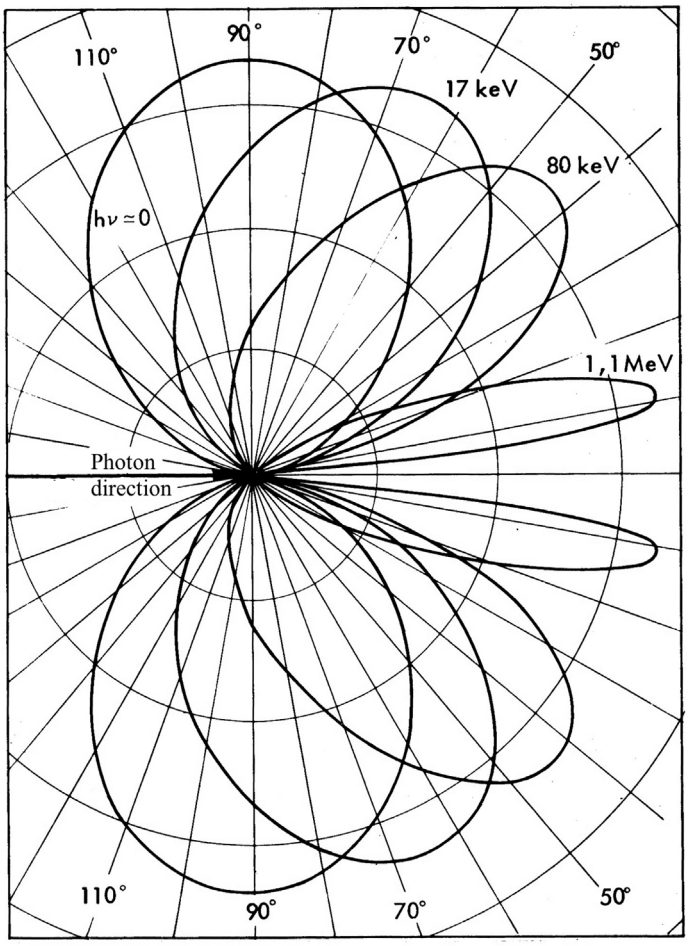

Figure 3.20 Angular distribution of photoelectrons for increasing values of the photon energy (Amaldi, 1971). By kind permission of the author.

electrons are produced by the Auger mechanism, with total energy close to E_k. Fluorescence photons, emitted at energy just below the K-edge, have a long mean free path for absorption; they can be locally reconverted, or flee the detection volume and be absorbed on the electrodes. This produces the characteristic escape peak of argon, at an energy around E_0 - E_k. In position-sensitive detectors the emission and reconversion of a long-range photon within the sensitive volume can introduce a large error if the position is estimated by measuring the centre of gravity of the detected charge. A quantitative discussion on this effect for xenon-filled counters can be found for example in Bateman *et al.* (1976).

Depending on its energy, the primary photoelectron is emitted in a preferential direction, as shown in Figure 3.20 (Amaldi, 1971); up to a few tens of keV,

https://doi.org/10.1017/9781009291200.005 Published online by Cambridge University Press

the direction of emission is centred around the perpendicular to the incoming photon direction, while at increasing energy the emission points towards the forward direction. As discussed in Chapter 2, however, multiple scattering on the gas molecules quickly randomises the motion of the heavily ionising photo-electron, and spreads the released charge around the interaction point. The range of electrons in gases was also discussed in the previous chapter.

Similarly to the case of charged particles (Section 2.1), the number N of electron–ion pairs released in a gas by a converted X-ray can be estimated by dividing the total energy loss (the photon energy in case of a complete absorption) by a phenomenological quantity W_{i}, energy per ion pair, whose value depends little on the gas, energy and nature of the primary ionizing particle;

$$N = \frac{E_x}{W_{\mathrm{i}}}. \tag{3.14}$$

However, while for charged particles the statistics of the energy loss is dominated by the Landau fluctuations, due to rare but very energetic encounters, for X-rays the constraint imposed by a maximum energy loss that cannot exceed the photon's total available energy modifies the statistics over a simple $\sqrt{N}$ dispersion. The process, first described in the early sixties (Fano, 1963) results in a reduction of the fluctuations, and is expressed by a gas-dependent quantity called the Fano factor; the statistical fluctuation in the number of ion pairs is then written as:

$$\sigma_N = \sqrt{FN} \tag{3.15}$$

with $F \leq 1$. Theoretical values of the Fano factor have been computed for noble gases and their mixtures, and measured for a wide range of other gases (De Lima *et al.*, 1982; Dias *et al.*, 1991; Doke *et al.*, 1992; Pansky *et al.*, 1993; do Carmo *et al.*, 2008); its value is particularly low in Penning mixtures, where a fraction of the energy loss spent in excitations can reconvert into ionization. As the values of W_{i} and F are correlated, they are usually estimated together. Table 3.1 is a

Table 3.1 *Average energy per ion pair and Fano factor for some gases (Sipilå, 1976).*

Gas	W_{I} (eV)	F (theory)	F (exp.)
Ne	36.2	0.17	
Ar	26.2	0.17	
Xe	21.5		≤ 0.17
Ne+0.5% Ar	25.3	0.05	
Ar+0.5% C_2H_2	20.3	0.075	0.09
Ar+0.8% CH_4	26.0	0.17	0.19

https://doi.org/10.1017/9781009291200.005 Published online by Cambridge University Press

representative summary (Sipilå, 1976); values can differ sometimes substantially depending on sources.

As will be discussed in Section 7.5, the value of F sets a statistical lower limit for the achievable energy resolution of counters, and has therefore extensively been studied in the development of high resolution X-ray detectors, and in particular the gas scintillation proportional counter (Policarpo, 1977).

3.7 Compton scattering and pair production

For photon energy above the highest electron shell level, Compton scattering becomes the dominant process. Quantum-mechanical theory describes the differential cross section and angular distributions of the interaction, see for example Evans (1958) and Davisson and Evans, (1952). The incident photon with energy E_0 is scattered by a quasi-free electron at an angle θ and energy E_1, while the electron emerges with an energy E_0 - E_1 at an angle ϕ, related by the expressions:

$$\frac{1}{E_1} - \frac{1}{E_0} = \frac{1 - \cos\theta}{mc^2}, \tag{3.16}$$

$$\cot\,\phi = \left(1 + \frac{E_0}{mc^2}\right)\tan\frac{\theta}{2}. \tag{3.17}$$

Except for very thick and dense detectors, it is unlikely for the scattered photon to be absorbed again in the same counter; the energy deposit depends therefore on the (generally unknown) angle of scattering, and no energy resolution is achievable in the Compton region.

The direction of the photon can be determined with a method named double Compton scattering. With reference to Figure 3.21 (left), the incident photon interacts in a first position-sensitive detector, recording the energy and coordinates of the recoil electron; the scattered photon interacts again in a following detector, providing energy and coordinates of the second Compton electron. Combining the previous expressions for the double scatter event, one can deduce the angle φ between the primary and scattered photons:

$$\varphi = \sin^{-1}\left(1 - \frac{m_0c^2}{E_2} + \frac{m_0c^2}{E_1 + E_2}\right); \tag{3.18}$$

the source has to lie then on a circle subtending an angle φ from the line joining the two scattering points. For a point source, the intersection of two or more circles determines its position (Figure 3.21 right).

The double Compton scattering method is exploited in astrophysics to determine the location of gamma sources, and in medicine for single photon emission

https://doi.org/10.1017/9781009291200.005 Published online by Cambridge University Press

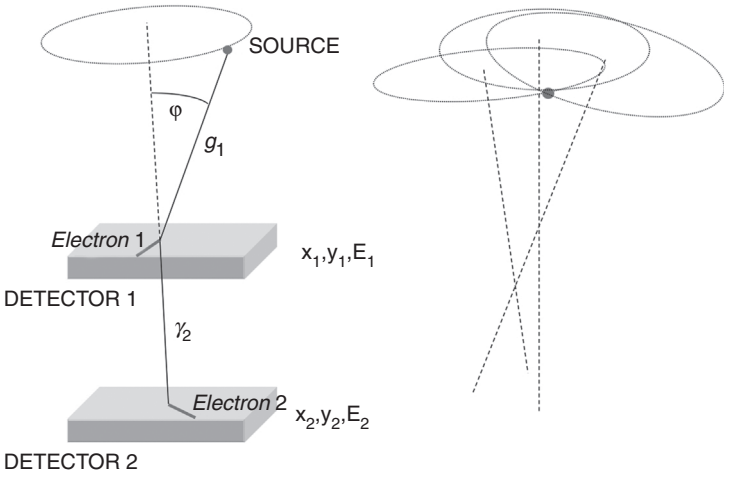

Figure 3.21 Principle of the double Compton scattering method.

tomography (SPECT) imaging; normally implemented with high density solid state detectors to achieve good efficiency, it is used also with liquid noble gas detectors (Section 15.2).

Electron–positron pair production can take place by an interaction in the nuclear field of materials at photon energies above the threshold energy of 1.02 MeV, corresponding to twice the electron mass; at high incident energies, the electrons and positrons are emitted mostly in the forward direction.

Both for Compton scattering and pair production, the probability of interaction in a gas counter is generally too small to be exploited for detection, but can take place on the counter walls or on suitably added converters. Electromagnetic shower counters are either constructed sandwiching chambers with conversion plates, or by using high-density drift chambers with suitable conversion electrodes in the gas volume itself.

3.8 Use of converters for hard photons detection

Due to the fast decreasing cross section, gaseous devices are not useful for detection of photons above a few tens of keV. Various methods of enhancing the efficiency at higher energies have been devised, making use of internal thin converters, particularly in view of applications in portal imaging and positron emission tomography. The conversion can be achieved with a stack of insulated metallic grids at suitable potentials, as in the high-density drift chamber (Jeavons *et al.*, 1975), with stacks of multi-wire proportional chambers having high-Z cathodes (Bateman *et al.*, 1980), sets of resistive plate chambers (Blanco *et al.*, 2003) or multi-electrode structures using gas electron multiplier (GEM) detectors (Iacobaeus *et al.*, 2000).

https://doi.org/10.1017/9781009291200.005 Published online by Cambridge University Press

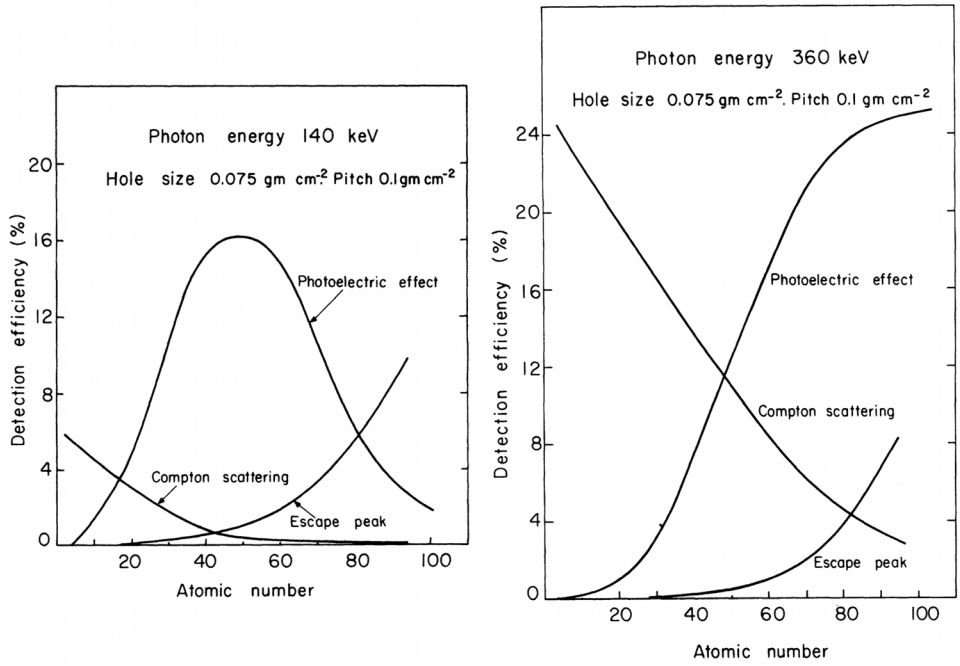

Figure 3.22 Detection efficiency of the heavy drift chamber as a function of the converter's atomic number, computed for 140 and 500 keV photons (Jeavons and Cate, 1976). © IEEE Transactions on Nuclear Sciences.

Depending on the converter material and photon energy, the detectable yield is an electron created by photoelectric effect or Compton scattering. While the conversion efficiency increases with the electrode thickness, the probability of the electron reaching the gas and being detected decreases; for each material and photon energy there is therefore an optimum thickness of the converter above which the efficiency remains constant.

Due to the higher ejected electron energy and the absence of scattered photons, which can reconvert in the detector, best performances are obtained using a material with a high photoelectric to Compton ratio. Figure 3.22 (Jeavons and Cate, 1976) shows the computed detection efficiency of a high-density drift chamber as a function of atomic number, for 140 and 500 keV, resulting from the K-shell photoelectric effect and Compton scattering. The curve labelled 'escape peak' corresponds to the background due to the de-excitation of the K-shell from a first photoelectric interaction. For the highest photon energy, a good compromise is tungsten ($Z = 74$), used as converter in the high-density drift chambers developed for positron emission tomography applications (Jeavons, 1978).

Stacks of multi-wire proportional chambers (MWPCs) with thin (125 μm) lead cathodes have been use for a similar purpose; Figure 3.23 gives the measured

https://doi.org/10.1017/9781009291200.005 Published online by Cambridge University Press

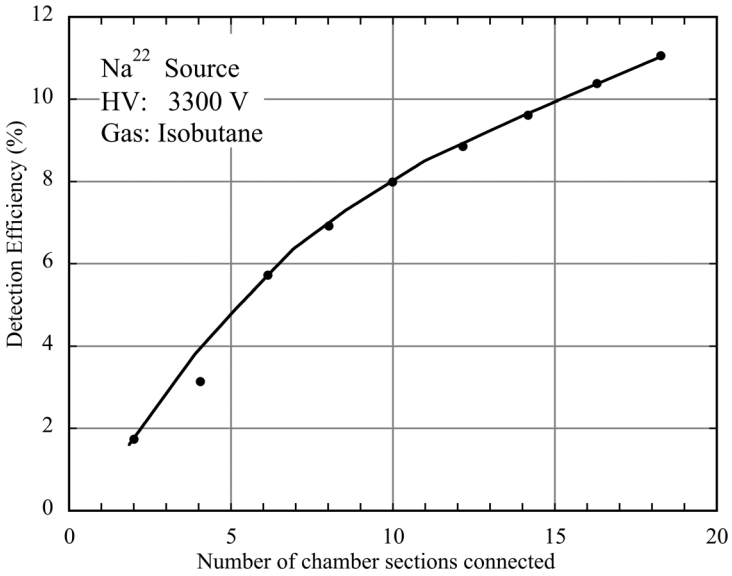

Figure 3.23 Detection efficiency for 511 keV photons as a function of the number of modules. Each module is a MWPC with 125-μm thick lead-coated cathodes (Bateman *et al.*, 1980). By kind permission of Elsevier.

detection efficiency for 511 keV photons as a function of the number of detector modules (Bateman *et al.*, 1980).

The intrinsically simpler design of resistive plate counters (RPCs), widely used in particle physics, has been adapted to the detection of hard photons. Figure 3.24 shows the computed efficiency of stacks of RPCs with lead and glass converters as a function of the converter thickness and number (Blanco *et al.*, 2009). While lead provides the highest efficiency, use of high-resistivity glass as converters and electrodes allows one to reduce the required number of readout channels, combining several detection elements in a single multi-gap resistive plate structure, an approach pursued by several groups, see Chapter 12.

The photon conversion efficiency of GEM detectors (Chapter 13) can be enhanced coating the active electrodes with a high-Z metal; Figure 3.25 shows computed and measured values of detection efficiency of a single detector with the electrodes coated with 3 μm of gold, as a function of photon energy (Koike *et al.*, 2011); multiple GEM structures can be used to increase the efficiency.

Metallic electrodes used in gaseous counters have a non-vanishing probability of ejecting a photoelectron when the incident photon energy exceeds their work function, typically between 4 and 5 eV (Fowler, 1931). Although in general not exploitable for detection, due to the very low efficiency, this process is often invoked to explain various kinds of internal photon-mediated secondary processes; sensitivity to external light sources as fluorescent lamps has also been observed.

https://doi.org/10.1017/9781009291200.005 Published online by Cambridge University Press

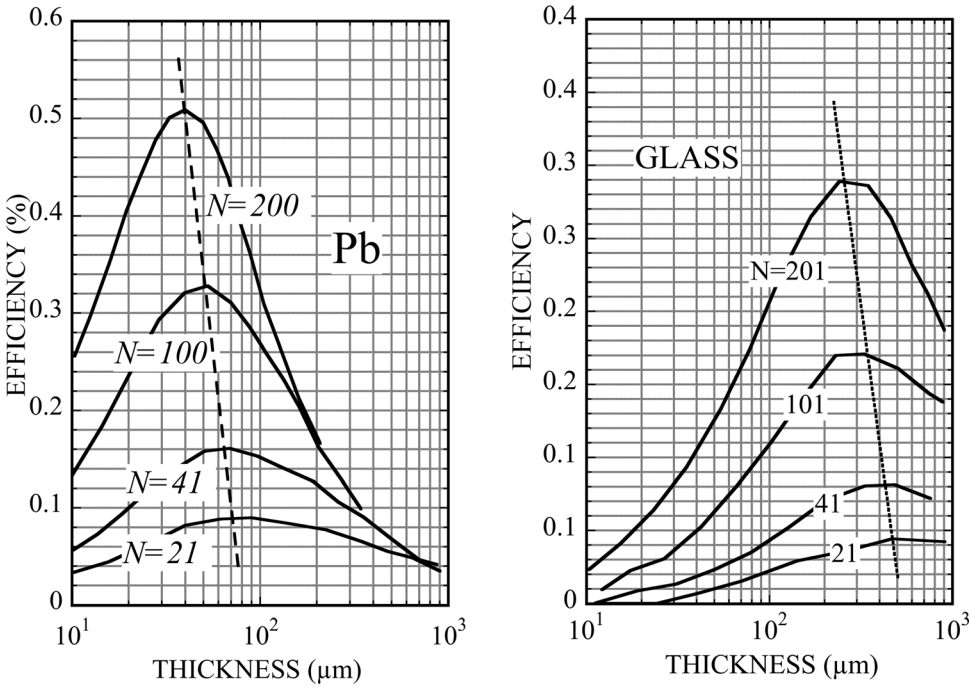

Figure 3.24 Detection efficiency for 511 keV γ rays as a function of thickness and number of conversion layers of lead and glass in a multi-gap resistive plate chamber (Blanco *et al.*, 2009). By kind permission of Elsevier.

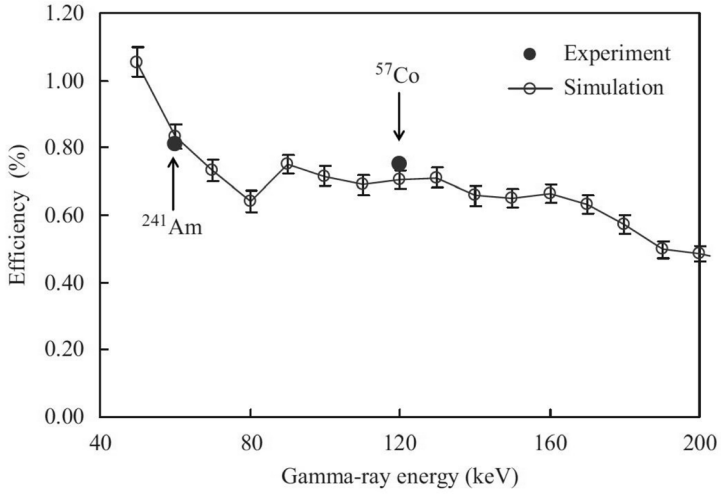

Figure 3.25 Computed and measured detection efficiency of a gold-coated GEM electrode as a function of photon energy (Koike *et al.*, 2011). By kind permission of Elsevier.

https://doi.org/10.1017/9781009291200.005 Published online by Cambridge University Press

3.9 Transparency of windows

To be detected, and unless they are emitted within the counter itself, photons have to enter the gaseous counters through a suitable window, where they can be partly converted; absorption losses depend on the window composition and thickness and on the energy of the photons. Figure 3.26 shows the transparency of several materials commonly used as windows for photon detectors in the visible and near ultra-violet, compiled from various sources. The region of sensitivity is the convolution of the window transparency and the quantum efficiency of the detecting medium, either in the gas phase or as internal photocathode. Examples of spectral response of several photosensitive compounds used in Cherenkov ring imaging detectors were given in Section 3.5; the high ionization threshold of TEA (7.5 eV) requires the use of expensive fluoride windows, while with TMAE or CsI a UV-quality quartz window permits the photon detection at lower energies.

The thin polyimide windows often used for gas containment because of their good mechanical strength have a rather low transparency cut-off, preventing most of the more energetic photons from entering the detector. Figure 3.27 shows the absorption length of mylar,[2] with a cut-off around 4 eV, and aclar,[3] a fluoro-polymer transparent at shorter wavelengths often added as second layer to reduce water absorption caused by the hydroscopic polyimides.

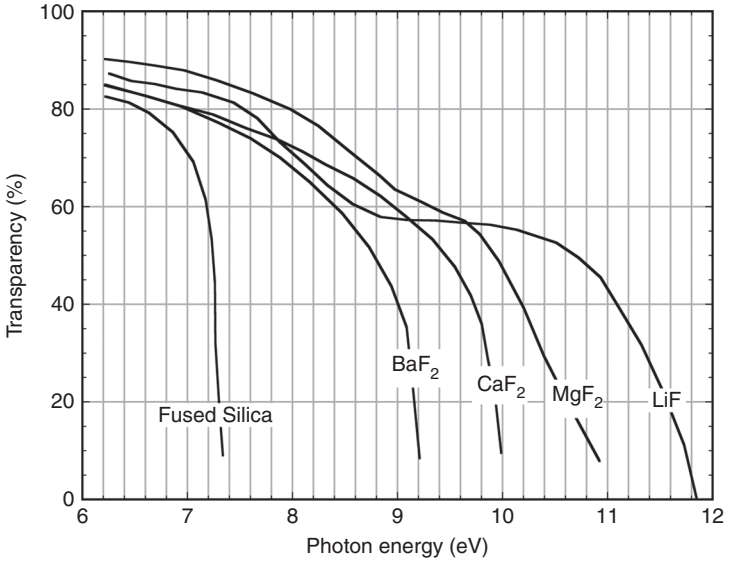

Figure 3.26 Optical transparency of fluoride and fused silica windows.

[2] DuPont polyethylene terephthalate [3] Polychlorotrifluoroethylene

https://doi.org/10.1017/9781009291200.005 Published online by Cambridge University Press

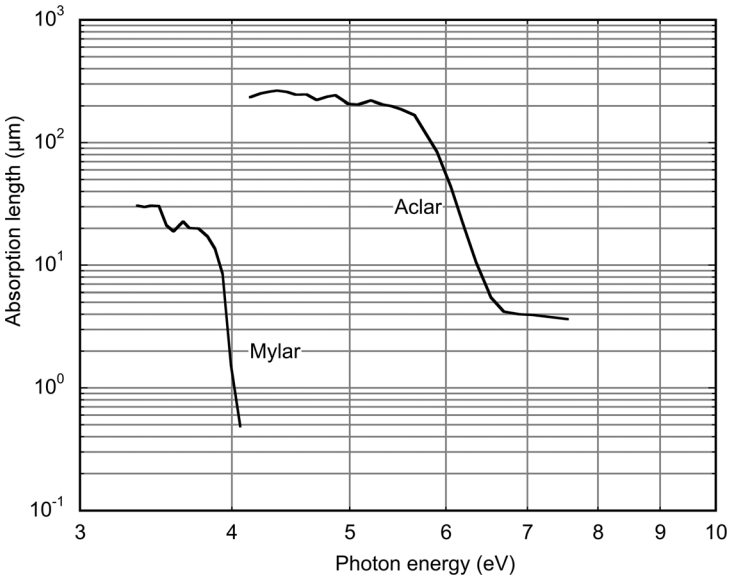

Figure 3.27 Absorption length of thin polymer windows in the near UV.

Figure 3.28 provides the computed absorption length of materials that can be used as detector windows in the soft X-ray domain, above 100 eV; the curves have the characteristic shape of photo-ionization processes, with the absorption length sharply decreasing on reaching the electronic shell levels of each component. The transparency of the window can then be estimated as a function of photon energy, using the expressions given in Section 3.2. Figure 3.29 gives an example, computed for beryllium and aluminium windows of different thickness.

3.10 Detection of neutrons

Neutrons interact with materials through several nuclear processes, with cross sections generally decreasing with energy. Only some major mechanisms leading to the creation of detectable signals will be discussed here; for an exhaustive coverage of the subject, see for example Knoll (1989). Extensive tables and plots of neutron cross sections can be found in Garber and Kinsey (1976).

Interaction processes and cross sections vary largely depending on materials and energy. The neutron energy, usually given in eV, is also expressed as wavelength in Å; the two units are related by the expression (Plank's law):

$$\lambda(\text{Å}) = 0.28601/\sqrt{E(\text{eV})}. \tag{3.19}$$

For high and intermediate-energy neutrons, above a few MeV, the major mechanism of interaction is elastic scattering, particularly efficient with low-atomic number materials, like hydrogenated compounds; while slowing down the

https://doi.org/10.1017/9781009291200.005 Published online by Cambridge University Press

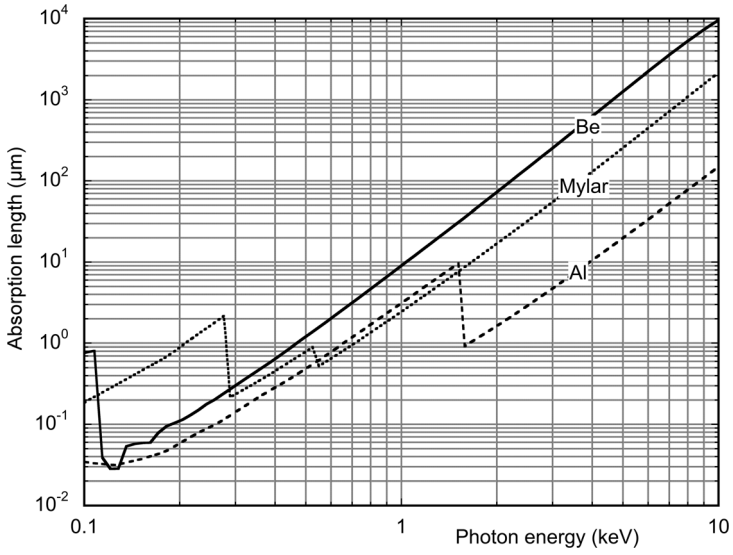

Figure 3.28 Absorption length of window materials for soft X-rays.

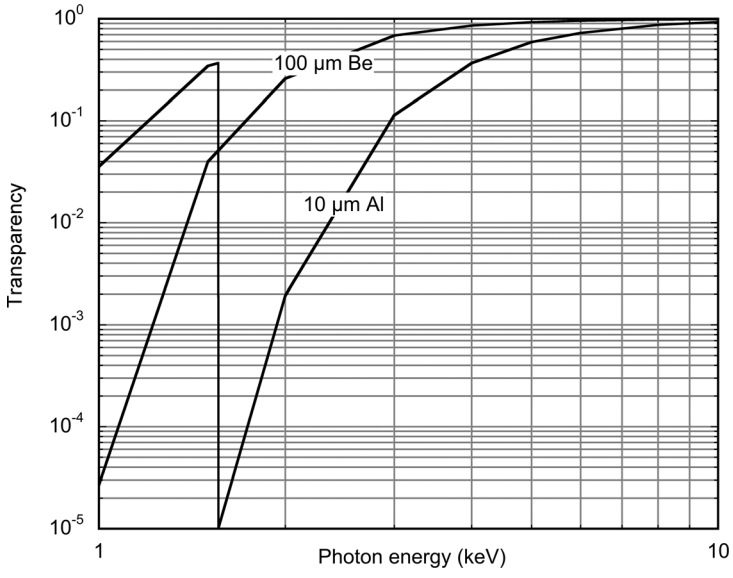

Figure 3.29 Transparency of thin metal windows for soft X-rays.

neutrons, in a process called moderation, elastic scattering does not provide a mean of detection. At energies around 1 MeV, inelastic scattering may occur, leaving the nucleus in an excited state that returns to the ground state through a radiative decay; this is the process exploited in activation devices. Around and below thermal energies, 0.025 eV, other nuclear interaction processes dominate; radiative capture and nuclear reactions with the emission of charged particles, protons,

https://doi.org/10.1017/9781009291200.005 Published online by Cambridge University Press

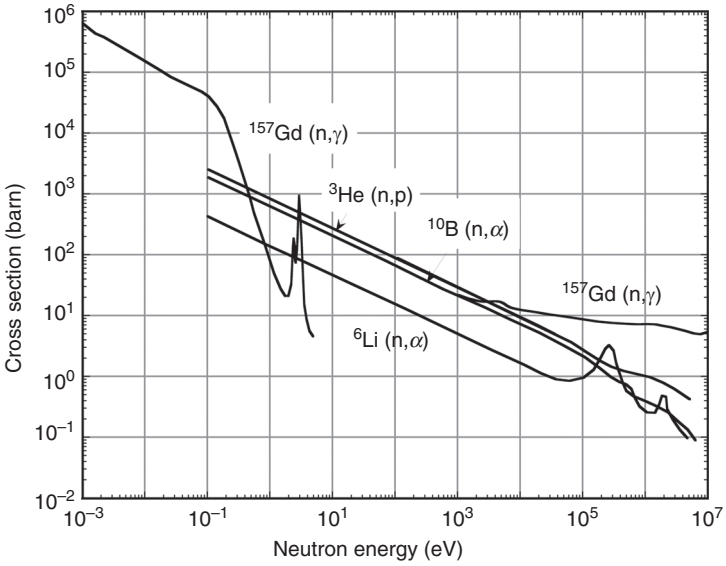

Figure 3.30 Neutron cross sections for several isotopes. Data from Garber and Kinsey (1976).

tritons, alpha particles and fission fragments, that can be detected directly. The detector itself can act as conversion medium; alternatively, thin converter foils surround a detection medium, such as a scintillator or a gaseous counter.

Figure 3.30 is a compilation of neutron cross sections as a function of energy for several elements commonly used for detectors (data from Garber and Kinsey, 1976). Gadolinium, while having the largest known capture cross sections for epithermal and thermal neutrons, results in the emission of prompt gammas and conversion electrons in the range between 30 and 180 keV, difficult to disentangle from the Compton scattered background. Several low atomic number isotopes have particularly large cross sections for thermal and low-energy neutrons; they result in the emission of heavy charged particles, which are easier to detect, can be used in the gas phase and are therefore widely used in detectors, through one of the reactions:

$$^{3}_{2}\mathrm{He} + n \rightarrow {}^{3}_{1}\mathrm{H} + p, {}^{10}_{5}\mathrm{B} + n \rightarrow {}^{7}_{3}\mathrm{Li} + \alpha \text{ and } {}^{6}_{3}\mathrm{Li} + n \rightarrow {}^{3}_{1}\mathrm{H} + \alpha.$$

The first process results in the emission in opposite directions of two ionizing prongs (triton and proton), with energies of 191 and 573 keV respectively, easily detected, and widely exploited in gaseous proportional counters. With a cross section of around 5000 barns at thermal energies, at atmospheric pressures the mean interaction length is around 10 cm (see expression (3.6)); higher efficiencies can be obtained by increasing the counter's gas pressure. An additional advantage of helium-filled counters is the reduced sensitivity to gamma rays, making their use suitable in mixed radiation fields.

https://doi.org/10.1017/9781009291200.005 Published online by Cambridge University Press

A systematic study of performances of ^{3}He-filled proportional counters can be found in Mills *et al.* (1962) and Ravazzani *et al.* (2006). A by-product of the nuclear power industry, the helium isotope has high costs and limited availability, making its use problematic for large detection volumes.

^{10}B-enriched boron trifluoride (BF_3) is used as gas filling in proportional counters (Fowler, 1973); the higher energy of the reaction products (840 keV for the lithium ion and 1.47 MeV for the α particle) makes their detection easier, but the efficiency is affected by the enrichment factor (natural boron contains around 20% ^{10}B isotopes). A comparison of performances of He and BF_3-filled counters can be found in Lintereur *et al.* (2011).

Detectors are designed to collect the ionization released by the interaction products; they can be positional, but do not provide information on the neutron energy. If the ionized trails have sufficient space extension, as in gaseous counters, detection and imaging of the yields can be exploited to provide information on the interaction vertex (see for example Fraga *et al.*, 2002; Miernik *et al.*, 2007). A long trail, however, has the drawback of being absorbed for part of the events on the counter's walls, resulting in a shift of the energy loss spectrum towards smaller amplitudes.

Alternatively to the use of absorbers in the gas phase, the neutron efficiency of conventional gaseous counters can be enhanced by the use of internal solid converters, deposited on the cathodes or on suitably segmented additional electrodes or baffles (Dighe *et al.*, 2003). Aside from boron, other converters used are thin layers of lithium, through the reaction ${}^{6}_{3}\mathrm{Li} + n \rightarrow {}^{3}_{1}\mathrm{H} + \alpha$, and ^{157}Gd, releasing low energy conversion electrons. As for photons, the detection efficiency is a convolution of the neutron reaction cross section and the probability of the reaction yield leaving the converter into the counter's gas; for boron and lithium, typical layers thickness of a few microns are optimal. As the two charged prongs in each event are emitted back to back, only one contributes to detection.

A systematic study of efficiency and optimization for thermal neutron counters with thin-film ^{10}B, ^{6}Li and ^{6}LiF coatings is given in McGregor *et al.* (2003); although the work aims at estimating the performances of solid state counters, most of the consideration apply to gaseous detectors. From the quoted reference, Figure 3.31 and Figure 3.32 show the computed residual energy of different ions as a function of the layer thickness, for neutrons perpendicular to a ^{10}B and ^{6}Li layer, and Figure 3.33 shows the estimated detection efficiency for both front and back irradiation. The calculation assumes full detector efficiency as far as a non-zero residual energy is lost in the active device. For thermal neutrons of two wavelengths, Figure 3.34 gives the calculated triton escape probability, forward, backward and total from ^{6}Li foils as a function of thickness (Dagendorf *et al.*, 1994).

Figure 3.35 (Klein and Schmidt, 2011) is an example of measured residual energy spectra measured for neutron irradiation in a gaseous counter

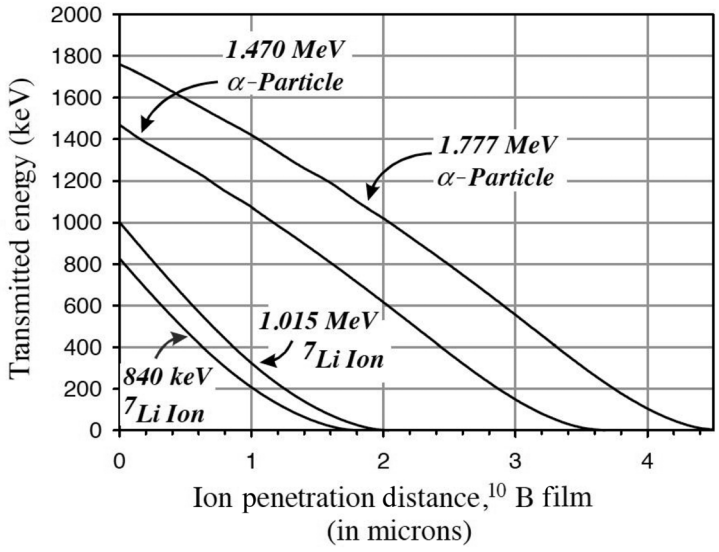

Figure 3.31 Residual energy for different reaction yields on ^{10}B as a function of film thickness (McGregor *et al.*, 2003). By kind permission of Elsevier.

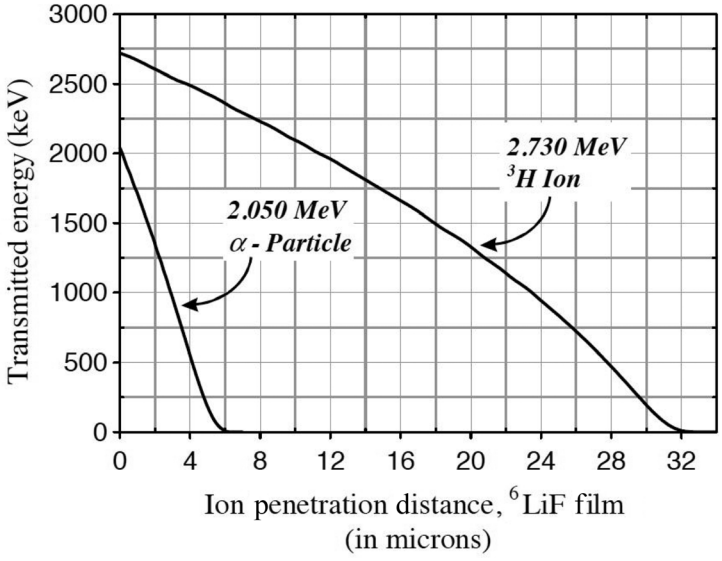

Figure 3.32 Residual energy for different reaction yields on ^{6}Li as a function of film thickness (McGregor *et al.*, 2003). By kind permission of Elsevier.

with 400 and 2300 nm-thick ^{10}B converters. For the thinner layer, the peaks correspond to the maximum energy of the prongs, tailing down to smaller values due to the energy loss in the converter; the degradation is more pronounced for the thicker layer.

https://doi.org/10.1017/9781009291200.005 Published online by Cambridge University Press

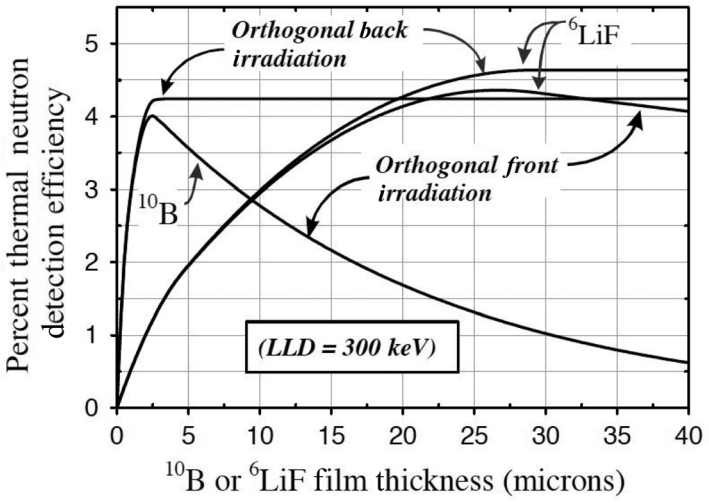

Figure 3.33 Thermal neutron detection efficiency computed as a function of conversion layer thickness, for perpendicular front and back irradiation (McGregor *et al.*, 2003). By kind permission of Elsevier.

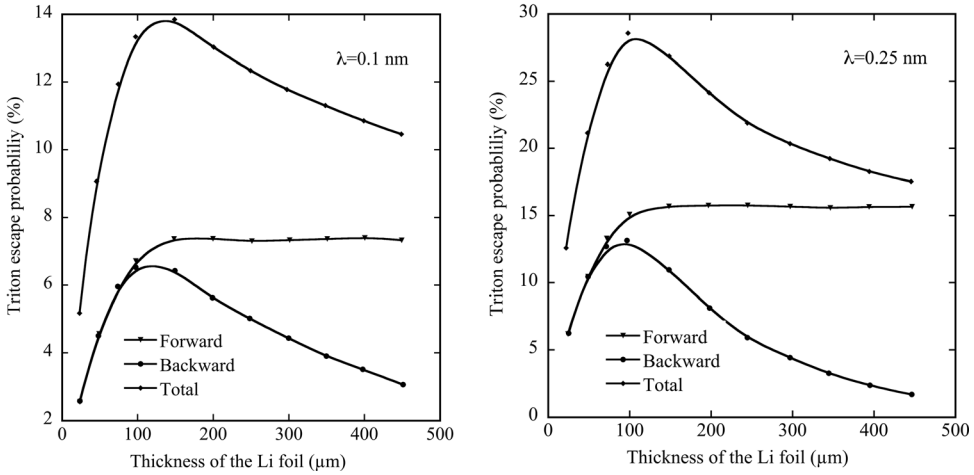

Figure 3.34 Triton escape probability from ^{6}Li converter foils at two neutron wavelengths (Dagendorf *et al.*, 1994). By kind permission of Elsevier.

The development of micro-pattern gas detectors (Sauli and Sharma, 1999; Titov, 2007), with their excellent localization and energy resolution, has enhanced the research on position-sensitive neutron detectors (see Chapter 13). In devices based on the gas electron multiplier, the multi-electrode structure can easily be optimized for neutron detection coating the electrodes with thin converter layers; Figure 3.36 (Klein and Schmidt, 2011) provides the expected detection efficiency of a

https://doi.org/10.1017/9781009291200.005 Published online by Cambridge University Press

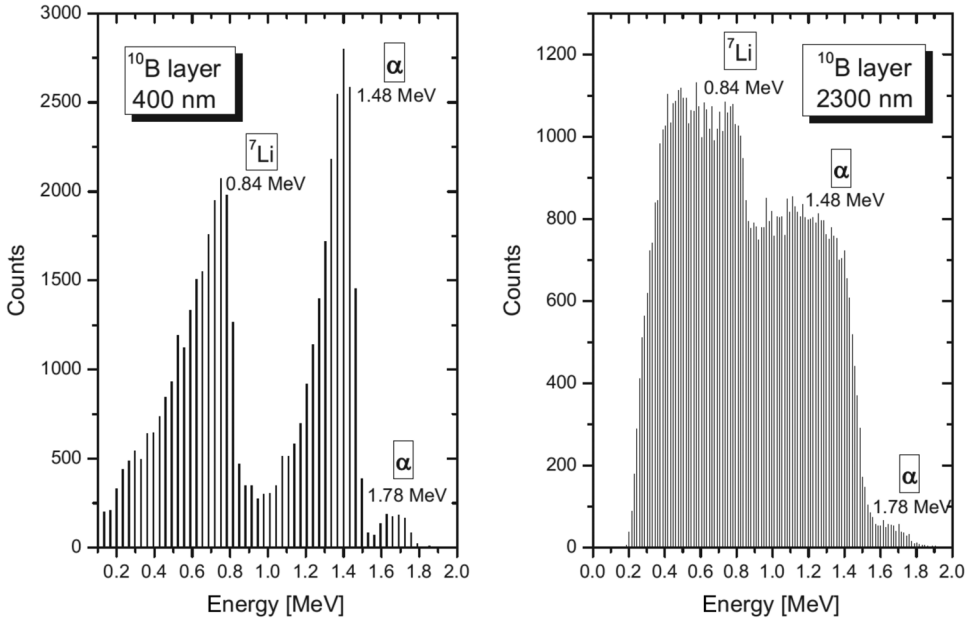

Figure 3.35 Measured neutron-induced residual energy spectra of the charged yields for two ^{10}B conversion layers, 400 and 2300 nm thick (Klein and Schmidt, 2011). By kind permission of Elsevier.

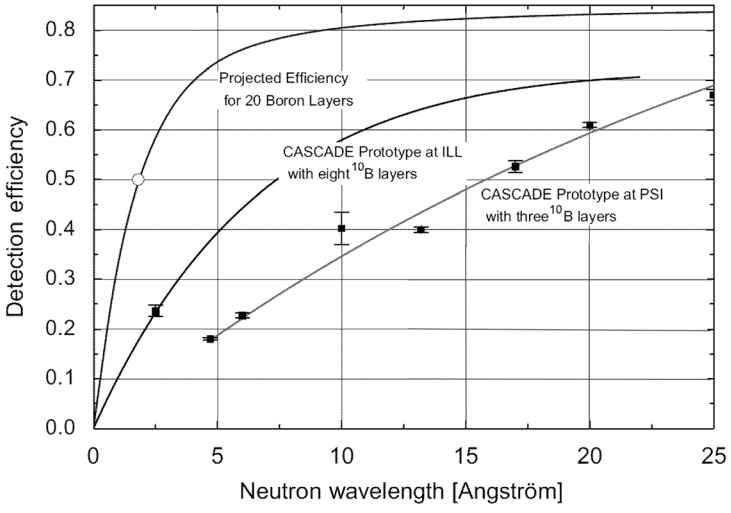

Figure 3.36 Computed efficiency as a function of neutron wavelength detector for multiple ^{10}B converter layers. Points with error bars are experimental measurements (Klein and Schmidt, 2011). By kind permission of Elsevier.

https://doi.org/10.1017/9781009291200.005 Published online by Cambridge University Press

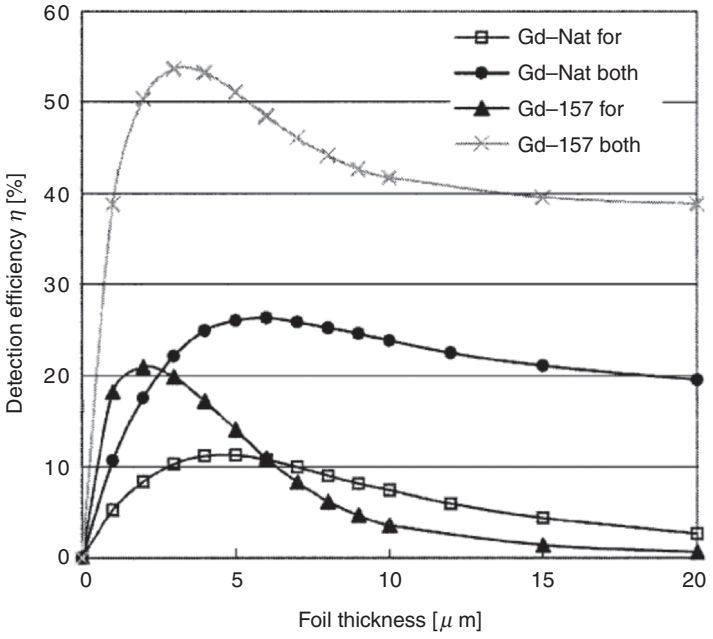

Figure 3.37 Detection efficiency for thermal neutrons as a function of thickness of natural Gd and ^{157}Gd. Values are given for all conversion electrons and for the forward fraction only (Masaoka *et al.*, 2003). By kind permission of Elsevier.

multi-GEM detector as a function of neutron wavelength for several choices in the number of layers; points with error bars are the measurements with three ^{10}B coatings, about 1.2 μm thick each. With a similar structure, using thin-foil natural Gd and ^{157}Gd Masaoka *et al.* (2003) have computed the detection efficiency for thermal neutrons as a function of converter thickness both for forward and total conversion electrons (Figure 3.37).

It should be mentioned that the copious neutron background usually met in high-energy physics experiments, unwillingly converted by the detector materials, has deleterious effects on the instrumentation: damages to materials and electronics and discharges in gaseous counters; this issue will be discussed in Chapter 16.

https://doi.org/10.1017/9781009291200.005 Published online by Cambridge University Press